Investigations into the influence of nickel loading on MoO₃-modified catalysts for the gas-phase hydrodeoxygenation of anisole†

Simon Haida, [iD] Sebastian Löbner, [iD] Henrik Lund, [iD] Stephan Bartling, [iD] Carsten Kreyenschulte, [iD] Hanan Atia, [iD] Ali M. Abdel-Mageed, [iD] Christoph Kubis [iD] * and Angelika Brückner [iD] *

Molybdenum oxide-based catalysts are promising catalysts for the gas-phase hydrodeoxygenation (HDO) of lignocellulosic pyrolysis oils with high selectivities to arenes. The gas-phase HDO is conducted at temperatures between 300 °C and 400 °C at ambient pressure, resulting in a low hydrogen consumption and high energy efficiency. The loading of nickel forming a binary structure consisting of MoO_3 and nickel molybdate ($NiMoO_4$) during calcination results in a significant increase of the catalytic activity connected with a drastic shortening of the induction period observed for the unpromoted catalyst system. The promotional effect of nickel seems to be related to its enhanced reduction behaviour and hydrogen dissociation leading eventually to an improved formation of a molybdenum oxycarbohydride phase (MoO_x-C_yH_z). The $MoO_xC_yH_z$ phase plays an important role in stabilizing active Mo^{5+} sites and prevents over-reduction to inactive MoO_2. The activity and benzene selectivity are maximal when pure $NiMoO_4$ is used as a catalyst. However, the selectivity towards undesired methane increases significantly indicating the decomposition of arenes. This effect is considerably reduced for catalysts with lower nickel contents (3–5%) which still exhibit a highly improved activity compared to MoO_3. *In situ* XRD studies revealed that the population of the $MoO_xC_yH_z$ phase is strongly affected by the nickel content, the structure of the hydrocarbon substrate and the hydrogen content during pre-reduction and catalysis.
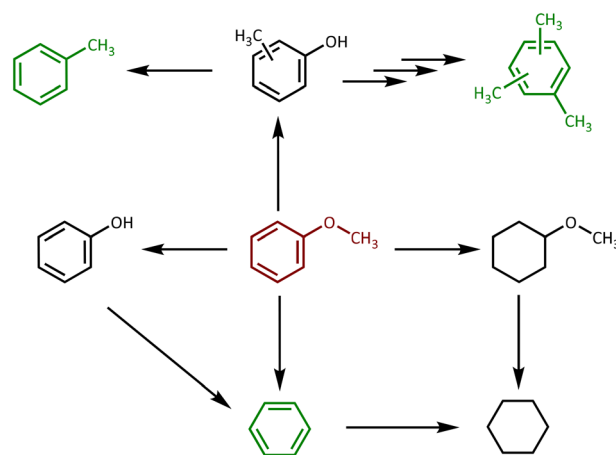
Introduction

Global warming and its consequences for our environment are one of the most challenging problems to date. For the development of a sustainable and circular economy a substitution of crude oil by renewable feedstocks is an important aspect.[1] One alternative feedstock to oil is lignin, as it is produced naturally in large amounts and can provide a wide range of different possible products.[2,3] Lignin is a complex polymer out of phenolic monomers of which the majority consists of sinapyl alcohol, coniferyl alcohol and *p*-coumaryl alcohol. For valorization, a pyrolysis step can be applied to convert biomass into its monomers, yielding a bio-oil. This can be performed by fast pyrolysis at T = 400–600 °C to obtain bio-oils in high yields.[4] However, due to the acidic properties of these pyrolysis-oils, there is a tendency for repolymerization. Further, their oxygen content is too high for direct usage as a feedstock for the production of fuels or chemicals.[5,6] Therefore, further process steps are required to reduce the oxygen content and thus gain a higher energy density. This can be achieved by the hydrodeoxygenation (HDO) reaction by using hydrogen. Apart from the utilization of respective products as renewable fuels, especially the production of BTX-aromatics (benzene, toluene and xylenes)

Leibniz-Institute for Catalysis e.V, Albert-Einstein Str. 29a, 18059 Rostock, Germany. E-mail: Christoph.Kubis@catalysis.de, Angelika.Brueckner@catalysis.de

Scheme 1 Hydrodeoxygenation of anisole to BTX-aromatics and selected possible by-products.

This journal is © The Royal Society of Chemistry 2024

*Catal. Sci. Technol.*, 2024, **14**, 2201–2217 | **2201**

seems to be an attractive route, as lignin is the most abundant polymer with aromatic rings in nature.[7,8] In Scheme 1 a simplified reaction path for the HDO of anisole, which is often used as a model substrate, to BTX-aromatics is presented.

The HDO reaction can be conducted in the liquid phase at moderate temperatures (200–400 °C) and higher partial hydrogen pressures (40–200 bar). The early generation of HDO catalysts consisted of typical hydroprocessing catalysts such as sulfided NiMo/Al$_2$O$_3$ and CoMo/Al$_2$O$_3$ or transition metal based catalysts.[9,10] Meanwhile, a large variety of catalyst types, *e.g.* supported mono- and bimetallic catalysts (noble and base metal based), supported and unsupported metal oxide catalysts (*e.g.* MoO$_3$) and nitrides and phosphides have been developed and tested.[11,12] Transition metal catalysts often show a high activity, but lower arene selectivity. In contrast, Mo based catalysts (NiMo, CoMo, MoO$_3$) tend to possess lower activities, but higher arene selectivities. Alternatively, the process can be operated at moderate temperatures (300–400 °C) but low hydrogen pressures ($p(H_2) \leq 1$ atm) in the gas-phase. This not only has the advantage of higher arene selectivity, but also the gas-phase HDO as a downstream process is an opportunity to use the energy of the previous pyrolysis step. Thus, a process design with an optimized energy balance is possible, as no cooldown and compression are necessary. Respective economic and ecological benefits should increase the overall process efficiency. Prominent catalysts which are investigated for gas-phase HDO are supported transition metal catalysts as well as pristine and promoted MoO$_3$. Due to the tendency of monometallic transition metal catalysts for ring hydrogenation, the arene selectivity is often relatively low. MoO$_3$ is an interesting alternative, as it shows good activity in the HDO reaction with comparatively high selectivity towards arenes.[12,13]

It is widely accepted that the catalytically active sites for MoO$_3$-based catalysts are Mo^{5+} ions, which are generated *via* partial reduction accompanied by the formation of oxygen vacancies at the surface of the catalyst on which the oxygenate substrate adsorbs *via* its oxygen atoms (Scheme 2a). The catalytic cycle of the HDO reaction can be described as a reverse Mars–van Krevelen type mechanism.[16–21] Several reports suggests also the *in situ* formation of a molybdenum oxycarbohydride phase (MoO$_x$C$_y$H$_z$) which seems to stabilize the oxidation state (v) of the molybdenum ions (Scheme 2b).[14,15,22,23] The mechanism of the formation of such a MoO$_x$C$_y$H$_z$ phase from MoO$_3$ in a hydrogen/hydrocarbon feed consists of several steps: 1) formation of MoO$_{3-x}$ *via* partial reduction and generation of oxygen vacancies, 2) formation of molybdenum oxyhydride (MoO$_x$H$_y$) by insertion of dissociated hydrogen into the solid, and 3) incorporation of carbon into the MoO$_x$H$_y$ intermediate to form MoO$_x$C$_y$H$_z$.[24,25] The dissociation of molecular hydrogen is catalyzed by MoO$_2$ which is partly formed during reduction. The presence of a transition metal might promote the formation of a MoO$_x$C$_y$H$_z$ phase because of its enhanced activity in hydrogen dissociation.[24] A significant over-reduction into MoO$_2$ (Mo^{4+}) leads to a significant decrease of catalytic activity. A MoO$_x$C$_y$H$_z$ phase cannot be formed from MoO$_2$ because its precursor molybdenum oxyhydride (MoO$_x$H$_y$) species are not formed from MoO$_2$. Coke formation is another important cause for the deactivation of HDO catalysts. A regeneration step consisting of *in situ* calcination followed by pre-reduction recovers the catalytic activity.[14]

Due to the importance of oxygen vacancies for substrate adsorption and activation, it is expected that changes in the electronic properties of the catalyst have a significant impact on the catalytic performance. To achieve this, oxide materials can be modified by the introduction of secondary metal atoms. For hydrodenitrogenation (HDN) and hydrodesulfurization (HDS), it was demonstrated that NiMoO$_4$ and CoMoO$_4$ have altered catalytic properties compared to bulk MoO$_3$. Also, it is known that the
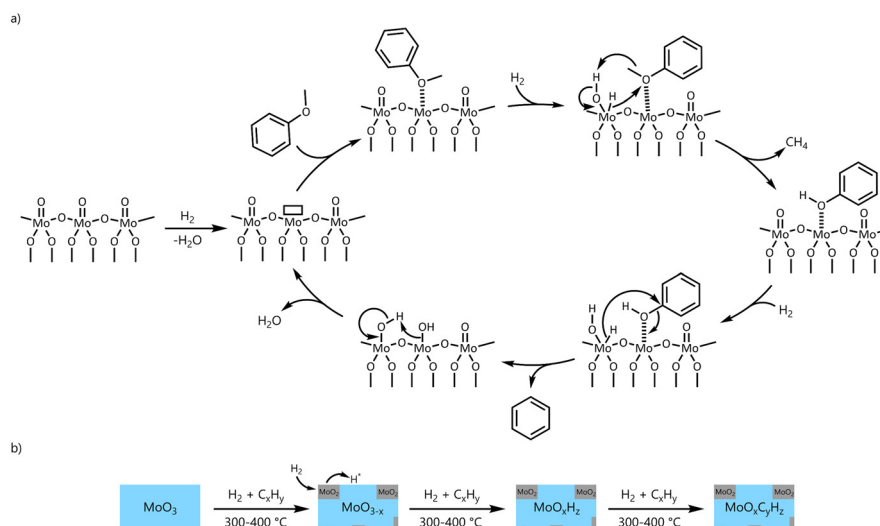
Scheme 2 a) Catalytic cycle of the hydrodeoxygenation of anisole based on the reverse Mars–van Krevelen type mechanism; b) sequence of phase transformation steps for the generation of a molybdenum oxycarbohydride phase (adapted and slightly modified from Richard *et al.* (a)[16] and Ledoux *et al.* (b)[24]).

2202 | *Catal. Sci. Technol.*, 2024, **14**, 2201–2217

This journal is © The Royal Society of Chemistry 2024

substitution of lattice metal atoms by low-valence dopants (LVD) does influence the redox properties of metal oxides and turn the oxide surface into a Lewis acid which in turn lowers the energy required for the formation of oxygen vacancies.[26,27] For HDO, there are several reports in which molybdenum oxide-based materials doped or modified by transition metals such as Ni, Co or Pt showed improved activities compared to pure MoO_3.[28–33] When nickel and cobalt are used as modifiers most often the respective metal molybdate phases ($NiMoO_4$ and $CoMoO_4$) are obtained after catalyst preparation and calcination.[29,32,34,35] Interestingly, no comparative studies have been performed to elucidate the impact of metal molybdate phases on catalyst performance and phase composition depending on their content.

Based on the discussed aspects *vide supra*, in this study we focus on the behavior of pure metal molybdates $NiMoO_4$ and $CoMoO_4$ as well as mixtures with minor amounts of these molybdate phases (1–5 wt% metal content) in a MoO_3 matrix in the gas-phase hydrodeoxygenation of anisole. The influence of the content of molybdate phases in MoO_3 on the catalytic performance and phase composition are investigated. A specific focus is laid on the formation and decomposition of a molybdenum oxycarbohydride phase ($MoO_xC_yH_z$) under the variation of reaction conditions for different catalysts. Structure–performance relationships are derived based on the results from *in situ* XRD, XPS and DRIFTS investigations leading to a comprehensive understanding of the promoting effect of metal molybdates on the catalytic HDO reaction.

Experimental section

Catalyst preparation

Commercial MoO_3 (Carl Roth, ≥98%) was used as a catalyst, as well as for the synthesis. For the synthesis of $NiMoO_4$ and $CoMoO_4$, 13.303 g (45.7 mmol) $Ni(NO_3)_2 \cdot 6H_2O$ (Sigma Aldrich, 99.1%) or 13.297 g (45.7 mmol) $Co(NO_3)_2 \cdot 6H_2O$ (Carl Roth, ≥98%), respectively, and 8.076 g (6.5 mmol) $(NH_4)_6$-$Mo_7O_{24} \cdot 4H_2O$ (Carl Roth, ≥99%) were dissolved in water. After complete solvation, the respective solution was stirred for 0.5 h and the water was evaporated at $T = 80$ °C afterwards. The sample was dried at 100 °C overnight and calcined at 450 °C for 5 h in syn. air. Samples with 1, 3 and 5 wt% content of Co or Ni were prepared by the same procedure using respective amounts of the components to achieve the desired metal content. An overview about the catalyst materials used in this study is given in Table 1.

According to the protocol of Glemser *et al.*,[36] MoO_xH_y was prepared by forming a suspension of 5.00 g MoO_3 and adding 1.8 g (27.5 mmol) zinc granules (Thermo Scientific, $d = 1$–5 mm, 99.999%). Hydrochloric acid was added 3.5 mL (4 N) and the mixture was stirred overnight. Afterwards, the suspension was filtered, the remaining zinc has been removed and the slurry was washed with deionized water until no chloride was detected with $AgNO_3$. The product was dried at 60 °C.

Table 1 Catalyst denotation

Description	ICP (M/wt%)	Denotation
Pure MoO_3	—	MoO_3
Pure $NiMoO_4$	27.34	$NiMoO_4$
Pure $CoMoO_4$	26.73	$CoMoO_4$
5 wt% Ni in MoO_3	4.91	$Ni(5)MoO_3$
3 wt% Ni in MoO_3	2.79	$Ni(3)MoO_3$
1 wt% Ni in MoO_3	1.02	$Ni(1)MoO_3$
5 wt% Co in MoO_3	4.73	$Co(5)MoO_3$

Catalyst characterization

PXRD. Powder X-ray diffraction (PXRD) patterns were recorded on a PANalytical X'Pert $\theta/2\theta$-diffractometer equipped with an Xcelerator detector using automatic divergence slits and Cu $K\alpha_1/\alpha_2$ radiation (40 kV, 40 mA; $\lambda = 0.15406$ nm, 0.154443 nm). Cu beta-radiation was excluded using a nickel filter foil. Finely pestled samples were mounted on silicon zero background holders. After data collection, obtained intensities were converted from automatic to fixed divergence slits (0.25°) for further analysis. Additionally, XRD powder patterns were recorded on a Stoe Stadi P transmission diffractometer equipped with a DECTRIs Mython2 1K detector applying Ge(111) monochromatized Mo $K\alpha_1$ radiation (50 kV, 40 mA, 0.70930 Å). The samples were ground to a fine powder and placed between two acetate foils before the measurement.

In situ XRD studies were performed on a Stoe Stadi P equipped with a Stoe ht2-*in situ* oven and a Mython 1K detector in Debye–Scherrer geometry using monochromatized Mo $K\alpha_1$ radiation (50 kV, 40 mA, 0.70930 Å). The sample investigated was ground, pressed to pellets at 10 tons, crushed, and sieved to fractions of 100–150 μm. A specimen was filled into a quartz glass capillary (approx. 2 mm outer diameter, 1 mm inner diameter, opened on both sides) until a height of approx. 6 mm was achieved and fixed using quartz glass wool. After mounting the capillary into the oven, the capillary was flushed with He (10 mL min⁻¹) and the sample was heated to the desired temperature (350 °C or 325 °C). After equilibration, the gas feed was changed to the reaction gas mixture (details in the corresponding description) with a total flow of 10 mL min⁻¹ and the reaction was monitored using static data collection over a 17° angular region (Mo-radiation). The gas dosage was determined using a set of Bronkhorst mass flow controller units. The applied temperature correction function was obtained by observation of well-known phase transitions ($AgNO_3$, $KClO_4$, Ag_2SO_4, SiO_2, K_2SO_4, K_2CrO_4, WO_3, $BaCO_3$). Peak positions and profiles were fitted with the pseudo-Voigt function using the HighScore Plus software package (PANalytical). Phase identification was performed by using the PDF-2 database of the International Center of Diffraction Data (ICDD). Because different X-ray sources were used (Mo, Cu, Ag), the diffraction data were converted to the Q-vector for comparison and representation purposes by using eqn (1).[37]

$$Q\text{-vector} = \frac{4\pi \cdot \sin(\theta)}{\lambda} \qquad (1)$$

This procedure gives diffractograms, which are independent of the used X-ray wavelength λ. The weighted average wavelengths were used for the Cu (1.54187 Å) X-ray source.

Raman spectroscopy. Raman spectra were recorded with a Renishaw inVia Raman microscope, equipped with a 633 nm laser and a Leica 50× objective. The used laser power was 0.085 mW with an exposure time of 10 s, with one accumulation.

SEM. Scanning electron microscopy (SEM) data were acquired using a Quattro S (Thermo Fisher) equipped with a Schottky emitter, a 60 mm^2 SDD detector (Thermo Fisher) for energy dispersive X-ray spectroscopy (EDS), a secondary electron (SE) detector (Everhart–Thornley type), and a back-scattered electron (BSE) detector (ring semiconductor type).

The specimen was dry deposited onto a Si wafer. The accelerating voltage was set to 10 kV for imaging and spectroscopy, with spot size selected for optimum resolution or current, respectively. Elemental maps were calculated from the spectral imaging data set using the net counts fitting method provided in the Pathfinder software (Thermo Fisher).

XPS. The XPS (X-ray Photoelectron Spectroscopy) measurements were performed on an ESCALAB 220iXL (Thermo Fisher Scientific) with monochromated Al Kα radiation (E = 1486.6 eV). Samples are prepared on a stainless-steel holder with conductive double-sided adhesive carbon tape. The measurements are performed with charge compensation using a flood electron system combining low energy electrons and Ar$^+$ ions (p_{Ar} = 1 × 10^{-7} mbar). The electron binding energies are referenced to the C 1s core level of carbon at 284.8 eV (C–C and C–H bonds). For quantitative analysis, the peaks were deconvoluted with Gaussian–Lorentzian curves using the software Unifit 2023. The peak areas were normalized by the transmission function of the spectrometer and the element specific sensitivity factor of Scofield. Details on the pseudo *in situ* XPS measurements are given in the ESI† (SI-A).

TG-MS. Thermogravimetric (TG) measurements were performed on a Sensys TG-DSC (Setaram, Caluire) coupled with an OmniStar quadrupole mass spectrometer (Pfeiffer Vacuum), scanning in the multiple ion detection (MID) mode. The MS ionization source was electron impact (EI) with an ionization energy of 70 eV. The samples were weighed ($m \approx 20$ mg) in open Al$_2$O$_3$ crucibles (100 μL) and heated from 25 °C to 600 °C in syn. air (20 mL min^{-1}) with a heating rate of 10 °C min^{-1}.

DRIFTS. *In situ* DRIFTS experiments were carried out with a Nicolet 6700 (Thermo Scientific) FTIR spectrometer equipped with an MCT detector and a Praying Mantis (Harrick Scientific) DRIFTS reaction cell. The dome of the reaction cell was mounted with CaF$_2$ windows. The setup was coupled with an online MS system (Omnistar GSD 320, Pfeiffer Vacuum) with a secondary electron multiplier for gas analysis. The samples were pressed and sieved to obtain a particle size of 250–315 μm. All samples were pre-reduced in pure H$_2$ (25 mL min^{-1}) for 2 h at 325 °C. For adsorption experiments of vaporized liquid substrates, they were pumped into an evaporator by a syringe pump (Harvard Apparatus, PHD ULTRA 4400) at a flow rate of 2.75 μL min^{-1} with a carrier gas (He) flow rate of 25 mL min^{-1}. The DRIFT spectra were registered with an optical resolution of 4 cm^{-1} with 64 scans per measurement. As a background spectrum, the spectrum of the pre-reduced catalyst at the experimental temperature under helium was used.

Catalytic testing

The catalytic test experiments have been conducted in a gas-phase packed-bed flow reactor. The tube reactor had an inner diameter of 11.9 mm which was fixed in a furnace. A thermocouple was used for temperature regulation and placed inside the catalyst bed. The catalyst material was pressed and sieved to achieve particle sizes between 600 and 800 μm. Before the catalyst was placed in the reactor held with quartz wool, 200 mg of the material was mixed with approximately 2.3 g of SiO$_2$ for diluting to a fixed volume. The SiO$_2$ had a particle size of 500–800 μm. The anisole was transferred into the reactor using a saturator where the H$_2$–N$_2$-mixture was flushed through. The saturator temperature was kept at 20 °C which results in a total anisole flow of 0.236 mL min^{-1} in the gas-phase and a WHSV = 0.31 g$_{anisole}$ g$_{cat}^{-1}$ h^{-1}. During the reaction, 40 mL min^{-1} N$_2$ and 20 mL min^{-1} H$_2$ at ambient pressure were used. Behind the reactor, 6.5 mL min^{-1} ethane was added as an internal standard. All gas flows have been controlled by Bronkhorst mass flow controller units. Prior to the addition of the substrate, the catalysts were heated up in N$_2$ to 325 °C and pre-reduced in 100% H$_2$ for 2 h at ambient pressure afterwards. After the pre-reduction step the catalysts were flushed with N$_2$ and bypass measurements were performed for feed analysis. The organic reactants and products were monitored continuously during the reaction on stream with an online GC (see technical details below).

Product analysis by online GC and calculation of performance data

The transfer line to the online GC system (Agilent 7890A) was kept at a temperature of 200 °C and the valve box of the GC was tempered at 210 °C. The sample loop had a volume of 250 μL. The GC column was a Quadrex 624 30 m × 250 μm × 2 μm. Helium was used as a carrier gas. The temperature program started at 40 °C for 2 min followed by heating up to 160 °C with 10 °C min^{-1} and a hold time of 5 min. Afterwards the oven was heated to 240 °C with 20 °C min^{-1} keeping the target temperature for additional 20 min. A FID was used as a detector.

The calculation of the conversion and selectivity is based on the corrected integral values of respective GC peaks using the "Effective Carbon Number Concept".[38] Thus, the integrals of the compounds were normalized by its corresponding response factor ECN (2).

2204 | *Catal. Sci. Technol.*, 2024, **14**, 2201–2217

This journal is © The Royal Society of Chemistry 2024

$$A_{ECN} = \frac{A}{ECN} \qquad (2)$$

The conversion (3) was determined using the area of anisole (i) and the average of bypass measurements. The area of the internal standard (IS) is included to account for possible volume changes during the reaction. The selectivity for the products (j) are given as carbon fractions (4).

Conversion

$$X = \left(1 - \frac{A_{ECN,i}}{A_{ECN,i,0}} \cdot \frac{A_{ECN,IS,0}}{A_{ECN,IS}}\right) \cdot 100\% \qquad (3)$$

Selectivity

$$S_j = \left(\frac{A_{ECN,j} - A_{ECN,j,0}}{A_{ECN,i,0} - A_{ECN,i}}\right) \cdot \frac{C\text{-atoms},j}{C\text{-atoms},i} \cdot 100\% \qquad (4)$$

Results and discussion

Selected material properties of fresh catalysts

Powder X-ray diffraction and Raman spectroscopy measurements were conducted to analyze the phase composition of fresh calcined catalyst materials (Fig. 1). The intense reflections of pure phase metal molybdates at 11 nm^{-1} and 21 nm^{-1} indicate the presence of NiMoO$_4$, while reflections at 17 nm^{-1} and 20.5 nm^{-1} prove the existence of the CoMoO$_4$ phase (Fig. 1a). For the nickel loaded catalysts (Ni(5)MoO$_3$, Ni(3)MoO$_3$ and Ni(1)MoO$_3$), the respective reflections assigned to NiMoO$_4$ can be observed at the same positions besides the major reflections from MoO$_3$. This observation indicates that a binary structure consisting of NiMoO$_4$ and MoO$_3$ is present. The same result was observed for the cobalt containing sample (Co(5)MoO$_3$) for which the CoMoO$_4$ phase has been identified.

These results were confirmed by Raman spectroscopy (Fig. 1b). The intense band for NiMoO$_4$ observed at 961 cm^{-1} is characteristic of this phase and is attributed to the symmetric stretching mode of the terminal M=O group.[39] At the same time, bands at 818 cm^{-1} and 993 cm^{-1} belonging to the MoO$_3$ phase are visible in the nickel loaded catalysts. The characteristic bands for the Mo–O–Co stretching vibration at *ca.* 937 cm^{-1} of CoMoO$_4$ are visible together with respective band contributions for MoO$_3$ in the cobalt containing catalyst.[40]

Catalytic results

Prior to the catalytic testing a pre-reduction step was conducted (325 °C, 1 bar H$_2$) for 2 h. The catalytic performance over 17 h time-on-stream (TOS) has been tested under atmospheric pressure at 325 °C for each catalyst revealing noticeable differences in their activity and product distribution (Table 2 and Fig. 2).

Catalyst activity and induction periods

For the unpromoted MoO$_3$ catalyst an induction period for *ca.* 5 h TOS was observed until the catalyst system reaches
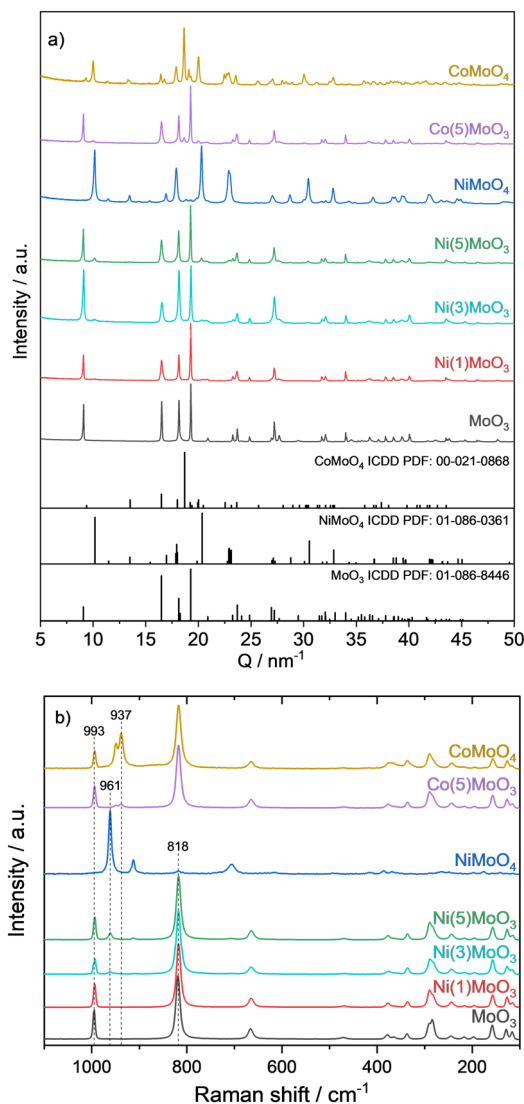

Fig. 1 Characterization of the fresh calcined samples. a) Normalized PXRD patterns; b) Raman spectra measured with a Renishaw inVia Raman microscope with λ = 633 nm and a laser power of 0.085 mW.

its maximum activity (equivalent to 37.7% conversion) followed by a moderate deactivation with time on stream. This type of catalytic behaviour is in accordance with previously reported results.[14] In contrast to this observation, the NiMoO$_4$ catalyst shows already in the beginning a very high activity with conversions of about 99% which only decreased slightly to 98% during the first 4 h. Surprisingly, no further deactivation is observed after reaching a steady-state within 6 h TOS until 17 h TOS. Compared to this behaviour, CoMoO$_4$ only reaches 41.6% conversion after an induction period of *ca.* 5 h TOS.

Ni(5)MoO$_3$ and Ni(3)MoO$_3$ are comparatively more active with conversions of 80.6% and 80.3% after 10 h TOS, respectively, without showing a distinct induction period and with only a low degree of deactivation. Conversely, for Ni(1) MoO$_3$ the maximum conversion drops to 59.0% (6 h TOS) after passing through a noticeable induction period.

This journal is © The Royal Society of Chemistry 2024

Catal. Sci. Technol., 2024, **14**, 2201–2217 | **2205**

Table 2 Anisole conversion and product selectivities (C-mol%) at 325 °C, WHSV = 0.31 $g_{anisole}$ g_{cat}^{-1} h^{-1} and TOS = 10 h. Selectivity ratio: S(arenes)/S(phenols) = R(A/P). Further data regarding the approximated overall carbon balance based on GC analysis (C yield) and the selectivity of uncalibrated unknown products are given in the ESI† (SI-B)

	X(anisole)	S(methane)	S(benzene)	S(toluene)	S(xylenes)	S(phenol)	S(cresols)	S(arenes)/S(phenols)
MoO_3	35.1	3.4	27.7	6.1	4.9	18.9	8.9	1.36
$NiMoO_4$	97.9	20.2	41.8	10.1	3.0	4.7	1.5	8.85
$Ni(5)MoO_3$	80.6	4.2	32.1	8.7	1.0	17.7	13.1	1.36
$Ni(3)MoO_3$	80.3	3.7	32.7	9.6	3.5	15.4	12.0	1.67
$Ni(1)MoO_3$	55.9	3.7	31.6	7.8	2.7	18.5	12.0	1.38
$CoMoO_4$	44.6	3.2	25.3	5.7	1.6	27.9	14.5	0.77
$Co(5)MoO_3$	49.3	3.6	27.8	5.6	2.0	28.9	16.1	0.79

Thereafter, a subsequent deactivation has been observed (55.9%, 10 h TOS).

The induction period for $Co(5)MoO_3$ is significantly longer (10 h) after which a conversion value of 50.0% is achieved. Interestingly, with ongoing time-on-stream the conversion increases slightly.

The pronounced induction periods for MoO_3, $Ni(1)MoO_3$, $CoMoO_4$ and $Co(5)MoO_3$ might indicate complex phase transformations which follow different individual time dependencies. For the unpromoted MoO_3 catalyst it is known from the literature that such an induction period is related to the formation of a $MoO_xC_yH_z$ phase.[14] It is assumed that the lattice carbon in the oxycarbohydride phase stabilizes the active Mo^{5+} oxidation state and hinders the over-reduction into less active Mo^{4+} sites.

Further aspects regarding the dynamics of the induction period are the pre-reduction step prior to substrate addition and the hydrogen to substrate ratio during the HDO reaction which effects the reducibility in the presence of the oxygenate substrate. The generation of $MoO_xC_yH_z$ is significantly improved when MoO_3 is pre-reduced in pure hydrogen at elevated temperatures (300–400 °C).[14,24,25]

Based on these considerations, one hypothesis for the absent induction period for $NiMoO_4$, $Ni(5)MoO_3$ and $Ni(3)MoO_3$ is the improved reduction behaviour, when nickel is present in significant amounts, which can promote the

$MoO_xC_yH_z$ formation proposed as an active intermediate (see discussion *vide infra*).[24] In this context, it seems likely that MoO_3 portions are reduced to a certain extent during the pre-reduction and the second step of partial carburisation is accomplished at such a short time scale, and that the effect of formation is not visible in the catalytic data.

The induction period of the cobalt containing catalysts might be caused by a much more complex reduction process of $CoMoO_4$ which can consist of several intermediate steps (*e.g.* $Co_2Mo_3O_8$ and $CoMoO_3$), which are not observed for $NiMoO_4$.[41] Possibly, the reduction temperature might not be high enough to reduce $CoMoO_4$ to Co^0, which could act as a hydrogen activator. In addition, the hydrogenation capability of Co is lower compared to Ni, which will influence the activation of hydrocarbons. Which one of these properties dominates with respect to the catalytic performance is difficult to determine.

Product selectivity

For the unmodified molybdenum trioxide catalyst (MoO_3), the selectivity after 10 h TOS (Table 2) towards aromatic hydrocarbons is moderate with 27.7% (benzene), 6.1% (toluene) and 4.9% (xylenes). Phenolic intermediates were formed with selectivities of 18.9% (phenol) and 8.9% (cresol), which results in an S(arenes)/S(phenols) ratio (R(A/P)) of 1.36. The selectivity to methane of 3.4% is at a low level. Hydrogenation products such as cyclohexane or cyclohexenes were not detected. It is noted that product selectivities strongly depend on the exact reaction conditions such as temperature, hydrogen:substrate:catalyst ratios and residence times. A systematic study of the impact of respective parameters goes beyond the scope of this study. The product selectivity profiles over time are given in the ESI† (SI-B).

The cobalt containing catalysts $CoMoO_4$ and $Co(5)MoO_3$ showed similar selectivities in comparison to MoO_3, except the phenol and cresol selectivities which increased, resulting in a R(A/P) of ≈0.78 for both.

For $Ni(5)MoO_3$ and $Ni(3)MoO_3$, the content of aromatic products increased to *ca.* 32–33% (benzene), *ca.* 9–10% (toluene) and *ca.* 1–3% (xylene). However, as the selectivities to cresols increased, the R(A/P) for $Ni(5)MoO_3$ remained at the same level compared to MoO_3. $Ni(3)MoO_3$ showed a
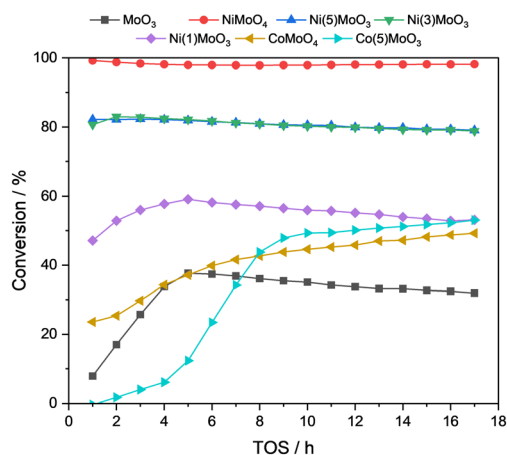

Fig. 2 Conversion of anisole HDO over 17 h TOS at 325 °C and P = 1 bar. Pre-reduced at 325 °C in 100% H_2 for 2 h.

2206 | *Catal. Sci. Technol.*, 2024, **14**, 2201–2217

This journal is © The Royal Society of Chemistry 2024

slightly increased $R(A/P)$ of 1.67. For $Ni(1)MoO_3$, the selectivity towards aromatic compounds dropped slightly while the selectivity to phenolic products increased compared to $Ni(3)MoO_3$ ($R(A/P)$ = 1.38). The selectivity to methane for these three nickel containing catalysts was *ca.* 4%.

Utilization of nickel molybdate $NiMoO_4$ leads to even higher selectivities towards benzene (41.8%) and toluene (10.1%) accompanied by lower values for the phenolic compounds. The low selectivity towards oxygenates leads to a high $R(A/P)$ ratio of 8.85. This could be explained by the high activity of $NiMoO_4$. Surprisingly, a very high value for the selectivity towards methane of 20.2% was obtained using this nickel molybdate catalyst.

Such a high methane selectivity for $NiMoO_4$ cannot be explained solely by the HDO of anisole, as it would provide approximately 14.2% methane for the selective reaction towards benzene. In addition, transmethylated products, *e.g.* xylenes, were obtained, which are formed by the C-transfer from the methoxy group followed by oxygen removal. From this it can be concluded that the aromatic ring must be decomposed to a significant extent. It can be assumed that besides the $MoO_xC_yH_z$ phase, other effects have an influence on the selectivity.

To test whether nickel has a dominant impact on the product selectivities, a catalytic control experiment was conducted with 3 wt% Ni on α-Al_2O_3. This catalyst showed, after 10 h TOS, a conversion of 16.7% with a methane selectivity of 44.2% and benzene selectivity of 25.8% (SI-B, Table SI-8†). In comparison to the performance data obtained for $Ni(3)MoO_3$ (Table 2), it is shown that the selectivity and activity is not dominated by Ni but by a molybdenum species. Further, for the Ni/α-Al_2O_3 catalyst a strong deactivation was observed starting with a conversion of 55.0% at 1 h TOS decreasing to 11.0% after 17 h TOS. Such a deactivation behaviour was not observed for the $Ni(X)MoO_3$ catalysts.

Characterization of spent catalysts

The spent catalysts were analysed by XRD, TG-MS, SEM and XPS to gain a better understanding about the respective phase compositions. BET surface areas (SA) have been determined as well for selected spent catalyst materials and no significant increase was observed compared to the fresh ones (SI-C†). For MoO_3 the SA increased from 3 m^2 g^{-1} to 7 m^2 g^{-1}. For $Ni(5)MoO_3$ the SA was increased during the reaction only from 15 m^3 g^{-1} to 18 m^2 g^{-1}, while for $NiMoO_4$ a decrease from 40 m^2 g^{-1} to 32 m^2 g^{-1} was found. This indicates that SA effects are perhaps not crucial for the altered catalytic performance between unpromoted and promoted catalysts.

Nevertheless, for $Ni(5)MoO_3$, scanning electron microscopy (SEM) gave evidence for the increased SA for nickel containing systems (SI-D, Fig. SI 8 and 9†). For the fresh sample, it was observed that a binary structure of small scale $NiMoO_4$ combined with larger MoO_3 crystallites is present. While the MoO_3 crystallites form planar surfaces with sharp edges, the

$NiMoO_4$ phase is distinguished by a significantly rough surface. The analysis of spent $Ni(5)MoO_3$ showed that after the reaction the microstructure was not changed and has a comparable structure as the fresh catalyst.

XRD measurements were conducted after the reaction only for the unpromoted and the nickel systems because it is hardly possible to distinguish between all possible phases for the cobalt systems on the basis of their complex diffractograms.[41] The $MoO_xC_yH_z$ phase could be identified in each catalyst, except the $NiMoO_4$ sample (Fig. 3).

The respective reflections for this $MoO_xC_yH_z$ phase are clearly observable at 10.1 nm^{-1}, 22.9 nm^{-1}, 27.1 nm^{-1}, 31.5 nm^{-1} and 44.2 nm^{-1}.[24,25,48,49] This was expected for the unmodified MoO_3 catalyst, as such an oxycarbohydride phase was already identified for the HDO of oxygenates.[14,22] The reflections assignable to MoO_2 were identified as well. Interestingly, while no MoO_3 was found in all spent catalysts, the $NiMoO_4$ phase for the nickel containing systems is present. Also, for the pure nickel molybdate catalyst only the respective reflections for $NiMoO_4$ were observed in the spent specimen. The reflections for $NiMoO_4$ and $MoO_xC_yH_z$ phases tend to overlap and are not easily distinguishable. For $NiMoO_4$, no indication for the presence of a $MoO_xC_yH_z$ phase has been found by TG-MS as shown later. This together confirms that the formation of a $MoO_xC_yH_z$ phase occurred only for $Ni(5)MoO_3$, $Ni(3)MoO_3$, $Ni(1)MoO_3$ and MoO_3 in measurable amounts.

There are several possible reasons for the detection of the $NiMoO_4$ phase in the spent catalysts after 17 h TOS, although a considerable amount of reduced nickel species was expected. One option is the potential incomplete reduction of the bulk core. Another possibility is the lower reduction degree of the catalyst in the presence of anisole at 30 vol% hydrogen during the reaction compared to the pre-reduction step performed in pure hydrogen. Also, the cooling phase after the reaction with the remaining anisole inside the reactor could lead to reoxidation. The exposition of the
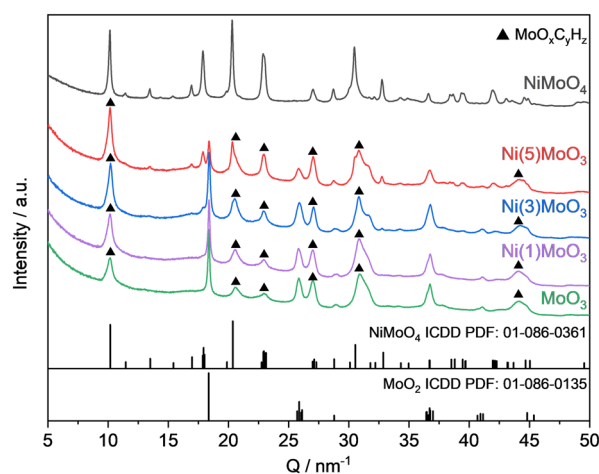

Fig. 3 Normalized XRD patterns of the spent catalysts after the HDO reaction of anisole for 17 h at 325 °C.

This journal is © The Royal Society of Chemistry 2024

Catal. Sci. Technol., 2024, **14**, 2201–2217 | **2207**

Paper

catalyst to air after demounting the reactor at elevated temperatures probably has an impact due to the pyrophoric properties of nickel.

To support our assignments with respect to the oxycarbohydride phase, TG-MS measurements have been conducted to check for deposited coke and the decomposition of the $MoO_xC_yH_z$ phase. For the spent $NiMoO_4$ catalyst the evolution of CO_2 starts at 350 °C with a small peak and a second one starting at 400 °C with its maximum at ≈440 °C but at the same time no correlated water formation can be observed (Fig. 4). It can be concluded that only graphitic coke is decomposed during the calcination and no or marginal amounts of $MoO_xC_yH_z$ are present in the sample. In comparison to this, the decomposition of a $MoO_xC_yH_z$ phase starting with fast CO_2 and water evolution at 380 °C and 400 °C is shown for MoO_3 and $Ni(5)MoO_3$, respectively. The decomposition of soft coke also takes place for $Ni(1)MoO_3$ and $Ni(3)MoO_3$ (SI-E, Fig. SI 10†). The amount of formed water should be correlated with the amount of the oxycarbohydride phase in the respective temperature regime. However, due to several experimental uncertainties regarding the possible lability when exposed to air, the quantification of the $MoO_xC_yH_z$ phase is hardly possible. Overall, these obtained results agree qualitatively with those obtained from XRD and indicate that Ni might have an influence on the formation and decomposition of the $MoO_xC_yH_z$ phase.

XP spectra of selected catalysts ($NiMoO_4$, $Ni(5)MoO_3$ and MoO_3) were recorded to elucidate surface properties and Mo oxidation states. The Mo 3d region was deconvoluted using three components Mo^{6+}, Mo^{5+} and Mo^{4+} using a similar fitting model to Murugappan et al.[15] For fresh calcined catalysts after preparation, almost exclusively, Mo^{6+} could be detected. This was concluded from the Mo $3d_{5/2}$ and Mo $3d_{1/2}$ doublet signals at $E \approx 232.6$ and 235.9 eV, respectively (Fig. 5).[42] Only for MoO_3 a minor fraction of approximately 2% Mo^{5+} ($E \approx 231.3$ and 234.4 eV) was found.

The spent catalysts showed significant differences with respect to their molybdenum oxidation states. The unmodified MoO_3 catalyst surface contains ca. 33% Mo^{6+}
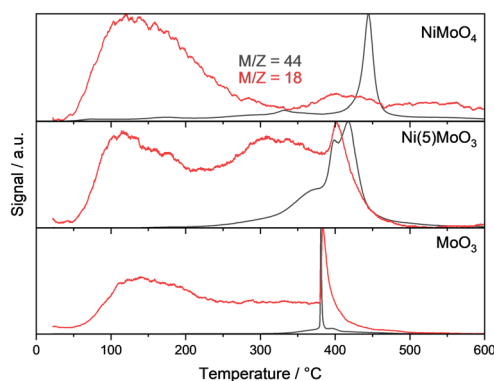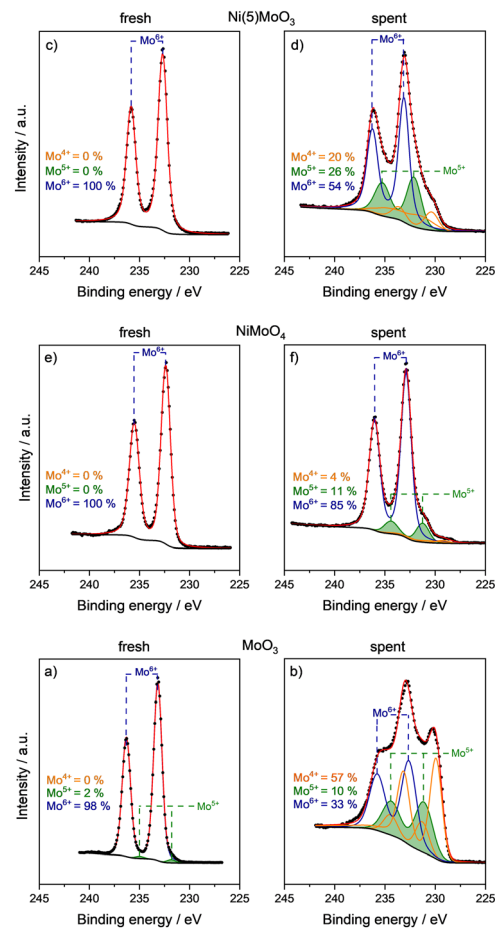

Fig. 5 Mo 3d XP spectra of the fresh and used catalysts after TOS = 17 h. a) Fresh MoO_3; b) spent MoO_3; c) fresh $Ni(5)MoO_3$; d) spent $Ni(5)MoO_3$; e) fresh $NiMoO_4$; f) spent $NiMoO_4$.

Fig. 4 Normalized TG-MS profiles of the spent catalysts treated in syn. air, 10 °C min⁻¹.

after 17 h TOS, while Mo^{5+} and Mo^{4+} were present with 10% and 57%, respectively. The fraction of Mo^{5+} is of special relevance since it is ascribed to be involved in the substrate activation. As already discussed, the formation of an oxycarbohydride phase can lead to the stabilization of Mo^{5+} sites. $Ni(5)MoO_3$ contained the largest fraction of Mo^{5+} (26%), and 54% Mo^{6+} and 20% $Mo^{4+}$are also observed. $NiMoO_4$ contained ca. 11% Mo^{5+}, 85% Mo^{6+} and 4% Mo^{4+}.

The increased amount of Mo^{5+} in $Ni(5)MoO_3$ is consistent with the results from the literature, in which for Ni and Co modified molybdenum oxide an enhanced accumulation of Mo^{5+} was reported.[28,29,32] It is surprising that the spent $NiMoO_4$ catalyst is reduced only to a small degree and the majority of the used material consists of Mo^{6+}, while it is expected that the reducibility is higher compared to pure MoO_3.[43] Nevertheless, the presented XPS data are in agreement with the XRD results, which showed the presence of $NiMoO_4$ as the major phase.

To study the reduction behaviour of the fresh catalyst materials in the absence of the anisole substrate, pseudo in situ XPS experiments were performed. The samples were treated at 325 °C and 1 bar of hydrogen for 2 h. The

2208 | Catal. Sci. Technol., 2024, **14**, 2201–2217

This journal is © The Royal Society of Chemistry 2024

reduction degree of Ni and Mo on the surface, of all three materials, was significantly higher compared with the spent catalysts in the expected order NiMoO$_4$ > Ni(5)MoO$_3$ > MoO$_3$ (SI-G, Fig. SI 13–17†).

The observed behaviour based on the molybdenum XP spectra is also reflected in the Ni 2p spectra of the spent and *in situ* treated nickel containing catalysts (Ni(5)MoO$_3$, NiMoO$_4$). The spectroscopic data are given in the ESI† (SI-F and G). For the spent catalysts, Ni^{2+} was identified as the major nickel species for each catalyst. Only for NiMoO$_4$ a small amount of Ni^0 was detected. For both catalysts, during the pseudo *in situ* reduction the formation of mainly Ni^0 was observed (SI-G, Fig. SI 16 and 17†). Additionally, H$_2$-TPR-experiments were carried out, where the results agree with the observed reduction behaviour based on *in situ* XPS in the absence of oxygenates where the reduction degree increases with the nickel content. Further details are given in the ESI† (SI-H, Fig. SI 18).

The most plausible explanation of the discrepancy between the XPS results of the spent and reduced catalysts is the reoxidation process which might take place due to the presence of an oxygenate substrate under a lower partial pressure of hydrogen during the reaction and/or the exposition to air in the course of disassembling the reactor. Further, water as a coupling product can cause a reoxidation. This effect might be especially relevant for nickel, which is known for its pyrophoric properties if being present in its metallic state with small particle size.

Adsorption behaviour of anisole and benzene

The adsorption behaviour of anisole (substrate) and benzene (product) was investigated by DRIFTS experiments. After heating up in a He flow to the reaction temperature (325 °C), the catalyst sample was reduced for 2 h in 100% H$_2$. Afterwards, the liquid component was injected into an evaporator (230 °C) using a syringe pump (2.5 μL min^{-1}) and the vapor was then introduced *via* gas-phase transport with He (25 mL min^{-1}) as a carrier into the DRIFTS cell. The flow was stopped after no intensity changes of the vibrational bands in the DRIFT spectra were observed. In the next step, the system was first flushed with He (10 min), and then the atmosphere was switched to H$_2$. After 5 min TOS, no major differences regarding respective band positions between the different catalysts were observed (Fig. 6).

In each system, the strong v(Ph–O–CH$_3$) vibrational band at 1251 cm^{-1}, the bands for v(C=C) at 1495 and 1600 cm^{-1}, and for v(CH$_3$) at 2842 cm^{-1} as well as bands for v(C–H) at around 3000–2850 cm^{-1} are visible.[44] In addition, each catalyst shows the formation of methane with a typical roto-vibrational band centered at 3016 cm^{-1}. The formation of methane is expected, because from a thermodynamic point of view, the hydrogenation of the O–CH$_3$ bond is favoured due to a lower binding energy compared to the Ph–OCH$_3$ bond. The bond dissociation energy (BDE) of the O–CH$_3$ bond is at about 424 kJ mol^{-1}.[12,45] However, the adsorption
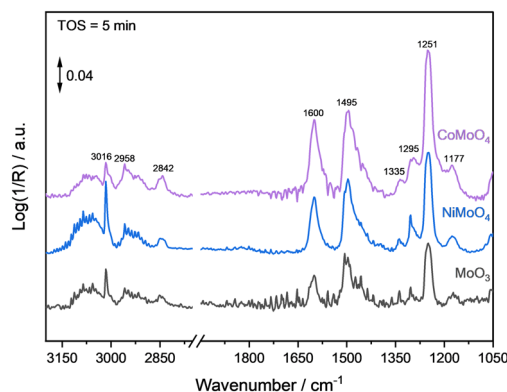

Fig. 6 DRIFT spectra of the catalysts with adsorbed anisole at 325 °C and H$_2$ (25 mL min^{-1}).

of anisole on each catalyst seems to be quite strong, as the decrease of the corresponding signals were slow (>40 min), see SI-I (Fig. SI 21†).

The relative integral values for the v(Ph–O–CH$_3$) vibrational band decreased to *ca.* 50% after *ca.* 20 min. Because the molybdenum oxide and metal molybdates form oxygen vacancies under reducing conditions, this strong adsorption behaviour can be expected for oxygen containing substrates (*e.g.* ethers, alcohols *etc.*).[16,46]

Besides the chemisorption of the educts, fast product desorption is crucial for active catalysts. Thus, the adsorption behaviour of benzene was tested following the same experimental procedure. Once the addition of benzene vapour was stopped after reaching stationarity in the DRIFT spectra, the respective vibrational bands of benzene started to immediately decrease for the MoO$_3$ catalyst (Fig. 7a). After four minutes of flushing with He, the vibrational bands nearly completely vanished, thus the majority of benzene seems to be desorbed. After the gas was switched to H$_2$, no changes in the DRIFT spectra could be observed (Fig. 7b).

For the NiMoO$_4$ catalyst the comparatively fast desorption of benzene was also observed (Fig. 7c). After four minutes of purging with He only very weak intensity bands at 3083 cm^{-1} and 3057 cm^{-1} (v(CH) vibrational bands) were visible. However, after switching to H$_2$ the roto-vibrational band of CH$_4$ centered at 3016 cm^{-1} was observed after 2 min (Fig. 7d). The band intensity increased further within an additional 2 min and after passing through a maximum it decreased slowly. A comparable behaviour was obtained for the CoMoO$_4$ catalyst. However, the evolution of methane started a few minutes later and a lower intensity for the band of methane was observed compared to the NiMoO$_4$ catalyst (SI-I, Fig. SI 19†).

Similar trends were also found in the online MS signals (m/z = 15) registered simultaneously during the DRIFTS measurements (Fig. 8). In the case of the NiMoO$_4$ catalysts, the formation of methane started immediately after H$_2$ was introduced into the system. The signal increased very fast and reached a short temporary plateau after about 3 min. The signal intensity increased further until a maximum
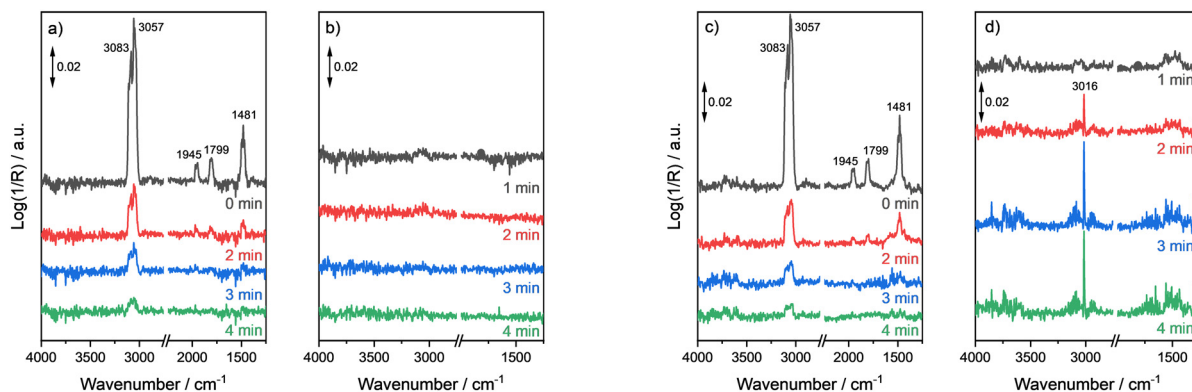
This journal is © The Royal Society of Chemistry 2024

Catal. Sci. Technol., 2024, **14**, 2201–2217 | **2209**

Fig. 7 a) Adsorption experiment of benzene in He on MoO_3 at 325 °C; b) switch to H_2 after benzene adsorption on MoO_3 at 325 °C; c) adsorption experiment of benzene in He on $NiMoO_4$ at 325 °C; d) switch to H_2 after benzene adsorption on $NiMoO_4$ at 325 °C.

appeared within 12 min. After going through the maximum, the methane evolution decreased over a longer period of more than 60 min. The $CoMoO_4$ catalyst behaved similarly with some minor differences. The first plateau was reached also after 3 min, but the intensity of methane evolution of this plateau is significantly lower compared to the $NiMoO_4$ catalyst. However, after *ca.* 20 min the maximum of methane evolution has reached a comparable intensity as for the $NiMoO_4$ catalyst, but its decrease appeared to be slower. Contrary to the DRIFTS results, also for the MoO_3 catalyst, methane formation could be observed, but to a significantly less extent compared to the metal molybdate systems. The maximum of the IC signal was reached after approximately 20 min and its intensity decreased slowly afterwards. Besides the molybdenum based catalysts, a control experiment with silica was performed to exclude other unknown methane sources. As expected, no methane formation was detected, and the signal remained very low.

The formation of methane after the adsorption of benzene is quite interesting as it seems that benzene is not just simply adsorbed on the catalyst surface but underwent some chemical conversion. To further prove the decomposition of aromatic rings with $NiMoO_4$ as a catalyst, a catalytic experiment in the fixed-bed reactor was performed with benzene as a substrate

Fig. 8 MS signal of methane evolution (m/z = 15) after benzene adsorption and switch to a H_2 atmosphere at 325 °C.

following the same protocol used for the HDO of anisole. The only products were methane and toluene and minor amounts of xylenes (SI-B, Table SI-9†). Note that the conversion is lower because of the increased WHSV compared to the experiments with anisole. However, the selectivity to methane of 21.0% after 10 h TOS is the same as found for the anisole HDO. With Ni(5) MoO_3 as a catalyst methane with a selectivity of 2.8% is also formed in the reaction with benzene under the applied reaction conditions (SI-B, Table SI-10†). One hypothesis for this behaviour could be the formation of a molybdenum oxycarbohydride phase ($MoO_xC_yH_z$) on a pre-reduced catalyst in the presence of benzene followed by the hydrogenolytic decomposition of this phase after the addition of hydrogen. As already mentioned, the appearance of a $MoO_xC_yH_z$ phase was described by Román-Leshkov *et al.* in the context of molybdenum oxide based HDO for the first time.[14] However, its formation was already published before by Ledoux and co-workers for alkane isomerization using MoO_3 as a catalyst.[47–49] This phase is formed at temperatures between 300 and 380 °C in a H_2/HC stream. To the best of our knowledge, there are no reports about such a phase in pure metal molybdates and only one for a cobalt promoted MoO_3 system.[32]

Several aspects with respect to the observed methane formation need to be considered. It is known that during the reduction of $NiMoO_4$ and $CoMoO_4$ the formation of a mixed-phase material occurs.[41,50,51] When $NiMoO_4$ is used, one fraction of metallic Ni and a second fraction of MoO_3/MoO_2 might be formed during the pre-reduction step. The molybdenum oxide phase could be transformed into the oxycarbohydride phase by the benzene/hydrogen mixture. Subsequently, hydrogen could be activated at the Ni center, which then diffuses to $MoO_xC_yH_z$ by hydrogen spillover.[25,29,52–54] This activated hydrogen could lead to the hydrogenation of carbon atoms and formation of methane (Scheme 3). However, the catalytic experiment under HDO conditions with Ni/α-Al_2O_3 as a catalyst and anisole as a substrate showed that nickel alone could decompose aromatic rings accompanied by the formation of methane. This was also proven by using benzene as a substrate in another catalytic control experiment (SI-B, Table SI-11†). It
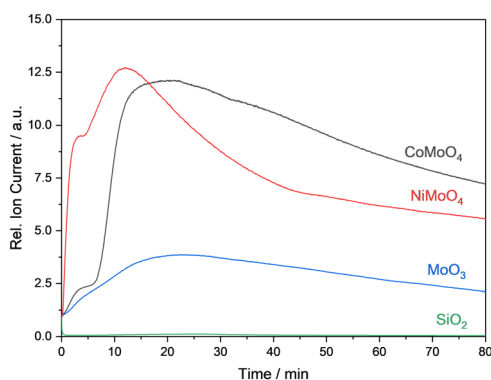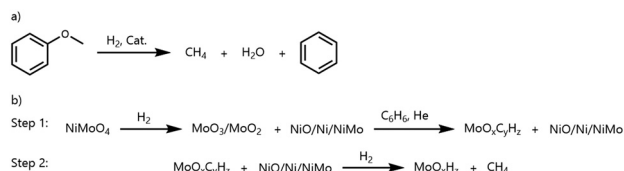
Scheme 3 Simplified scheme for a possible pathway of the methane formation on a nickel molybdate catalyst. a) CH_4 formation by the HDO reaction and b) CH_4 formation by $MoO_xC_yH_z$ decomposition.

can be concluded that both discussed events can occur at the same time and contribute to the high CH_4 selectivity with $NiMoO_4$.

Acidity properties and their relevance to the HDO reaction

The acidity properties of MoO_3 and $NiMoO_4$ were determined by NH_3-adsorption FTIR measurements. The samples have been pre-reduced in H_2 at 325 °C for 2 h to prevent differences between the analysis and HDO reaction. At room temperature, 5% NH_3 in He was pulsed on the samples until saturation. Afterwards, they were heated up to 300 °C and with 50 °C steps a spectrum was recorded.

Noticeable differences in the nature of the acidic sides between MoO_3 and $NiMoO_4$ have been observed (the spectroscopic data are presented in SI-J, Fig. SI 22–25†). MoO_3 shows a strong vibrational band at 1425 cm^{-1} which is assigned to Brønsted-acid (BA) sites.[55,56] Vibrational bands assignable to Lewis acid (LA) sites could not be detected.

For $NiMoO_4$ the vibrational band at 1425 cm^{-1} associated with BA sites can be observed as well, however it is significantly less intense compared to MoO_3. Additionally, vibrational bands related to LA sites at 3350 cm^{-1} and 3270 cm^{-1} can be observed up to 300 °C. These LA sites could play a role in the improved catalytic properties, as they can act as adsorption sites for the oxygen containing substrates. BA sites are involved in the hydrogenolysis of the substrate. $NiMoO_4$ combines both properties, while MoO_3 only has BA sites. In addition, the influence of LA sites on the formation of $MoO_xC_yH_z$ has been discussed in the literature before and could be beneficial for its formation.[32]

In situ XRD studies on the formation of $MoO_xC_yH_z$ phases

In situ XRD experiments were carried out to gain a deeper understanding of the $MoO_xC_yH_z$ phase formation and the effect of nickel on this formation.

Influence of the feed composition on the $MoO_xC_yH_z$ phase formation starting from MoO_3

To acquire profound knowledge on the reaction behaviour, the experiment series was started with the generation of $MoO_xC_yH_z$ in MoO_3 with a H_2/CH_4 gas mixture. Methane was chosen because it represents a well-defined gaseous hydrocarbon, suitable for long-term *in situ* XRD experiments. The temperature for this experiment was set to 350 °C, because it was initially not clear, whereas the lower

temperature used in the catalysis (325 °C) is sufficient for the formation of the $MoO_xC_yH_z$ phase from a less reactive substrate such as methane. However, it was expected that the generation of a molybdenum oxycarbohydride phase should be feasible, as it is reported in previous works that $MoO_xC_yH_z$ formation is possible with a variety of hydrocarbon substrates including *n*-alkanes and several oxygenates.[14,24,25,49,57] To understand the importance of the pre-reduction step for this phase formation and the influence of the H_2/CH_4 ratio, the ratio was systematically varied in the following order H_2/CH_4 = 9:1, 1:1, 1:9.

The series was started with a ratio of $H_2:CH_4$ = 9:1 and after the introduction of the reactive gas, the transformation of MoO_3 to MoO_2 was initiated. With some time-shift the appearance of reflections which can be duly assigned to a $MoO_xC_yH_z$ phase could be clearly observed at $Q \approx 27$ nm^{-1} and 31.5 nm^{-1} after *ca.* 200 min (Fig. 9). Those signals increased further over time within the entire investigated time span of 1200 min (SI-K, Fig. SI 26†).

To prove the assignment of the evolved new reflections to a $MoO_xC_yH_z$ phase, molybdenum blue was treated with $H_2:CH_4$ = 9:1 at 325 °C for 1200 min. Molybdenum blue is a pre-reduced MoO_3 which might consist of several MoO_xH_y intermediate phases and tend to selectively form a $MoO_xC_yH_z$ phase when treated with hydrocarbons. The material was synthesized as described by Glemser *et al.*[36] The obtained reflections assigned to the molybdenum oxycarbohydride phase for the *in situ* treated MoO_3 material are in agreement those obtained for the treated molybdenum blue (Fig. 9).

When the feed ratio was altered to $H_2:CH_4$ = 1:1, the observed trends were the same and the $MoO_xC_yH_z$ phase was formed after approximately 200 min. However, for the experiment with a feed ratio of $H_2:CH_4$ = 1:9 a completely
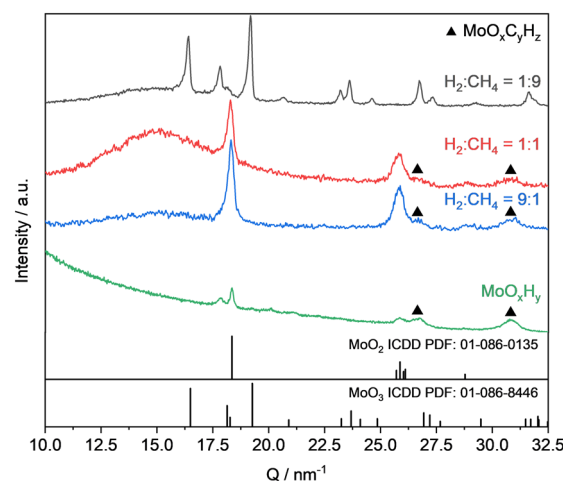

Fig. 9 Normalized *in situ* XRD patterns for the MoO_3 treatment at 350 °C in a H_2/CH_4 mixture (flow: 10 mL min^{-1}) at TOS = 300 min for $H_2:CH_4$ = 9:1 and 1:9, TOS = 305 min for $H_2:CH_4$ = 1:1. Note that the broad reflection at $Q \approx 15$ nm^{-1} belongs to the SiO_2 capillary reactor. *Ex situ* diffractogram for MoO_xH_y treated in $H_2:CH_4$ = 9:1 at 325 °C for 1200 min forming a $MoO_xC_yH_z$ phase (▲) for comparison with the *in situ* data.

This journal is © The Royal Society of Chemistry 2024

Catal. Sci. Technol., 2024, **14**, 2201–2217 | **2211**

different behaviour was found. In this case, the starting material MoO_3 was practically not reduced with no changes in the diffractograms between the starting and end point (SI-K, Fig. SI 28 and 29†). It can be concluded that a certain lower limiting amount of hydrogen in the feed is required for the reduction of Mo^{6+} to Mo^{5+} and the succeeding formation of the oxycarbohydride phase.

Formation of the $MoO_xC_yH_z$ phase with $NiMoO_4$ and Ni(5)MoO_3 as catalysts

In the next step, an *in situ* XRD experiment with $NiMoO_4$ was performed. The temperature was slightly lowered to 325 °C because a higher activity with respect to catalyst reduction was expected. Considering the methane evolution, observed in the DRIFTS experiments, a question was raised, whether the $MoO_xC_yH_z$ phase can be populated, is directly decomposed, or reached equilibrium when the treatment is not carried out stepwise. At the beginning, a reduction step with pure hydrogen was performed to get more insight into the reduction behaviour of $NiMoO_4$. For this sample after the reduction step for 120 min the dominant reflections are assigned to Ni and NiO (Fig. 10). The results from pseudo *in situ* XPS measurement of the reduction with hydrogen suggested that Ni^0 is the dominant nickel species on the surface (SI-G, Fig. SI 16†). Reflections with a lower intensity of MoO_2, which overlap in part with those of Ni, are also visible at $Q \approx 18.4$ nm^{-1}, 26.0 nm^{-1} and 36.7 nm^{-1} (Fig. 10).

When $NiMoO_4$ was treated with the H_2/CH_4 (1:1) gas mixture, the result is nearly identical. The only difference is the absence of the reflections which belong to the MoO_2 phase. Possible reasons for this absence could be a decrease in particle size and amorphousness compared to the nickel phases. It remains unclear whether a certain amount of a $MoO_xC_yH_z$ phase has been formed, for which also only weak and broad reflections (Fig. 9) are obtained.

In the next step, an *in situ* XRD measurement was carried out with the Ni(5)MoO_3 catalyst. Due to the low Ni loading of 5 wt% nickel phases (Ni, NiO) should not dominate the diffractogram. This system is of specific interest, because the material was much more efficient with respect to the catalytic performance regarding the HDO of anisole compared to MoO_3. The experiment was conducted in a modified stepwise manner. After a pre-reduction step for 2 h in hydrogen, the system was treated with methane for several hours. The reflections for the $MoO_xC_yH_z$ phase were visible after 150 min TOS directly after the switch to the CH_4 atmosphere (SI-K, Fig. SI 30†). It is noted that the respective reflection signals registered during the *in situ* measurements in the capillary were quite low in intensity. Therefore, a long-time scan measurement was performed afterwards (Fig. 11). The reflections at $Q \approx 27$ nm^{-1} and 31.5 nm^{-1} and 44.2 nm^{-1} also fully match with those acquired for the reference sample obtained from the molybdenum blue material (Fig. 9).

Even in the case when reflections from nickel species contribute to the overall diffractogram and overlap with those of the $MoO_xC_yH_z$ phase, the major contribution of the three most intense reflections should stem from the $MoO_xC_yH_z$ phase, since the Ni content is only 5 wt%. Besides these reflections, those for MoO_2 can also be observed at $Q \approx 26$ nm^{-1} and 37 nm^{-1}. Compared with the synthesis of the $MoO_xC_yH_z$ phase starting from MoO_3, the Ni(5)MoO_3 catalyst seems to form a significantly larger amount of the oxycarbohydride phase in agreement with an improved ratio between the integral values for $MoO_xC_yH_z/MoO_2$.

Effect of using more reactive propene instead of methane

The oxycarbohydride formation starting from MoO_3 was also investigated with propene to elucidate the effect of using a more reactive hydrocarbon compound compared to methane. It was found that not only the formation of the $MoO_xC_yH_z$ phase starts earlier, also a bigger portion of the $MoO_xC_yH_z$ phase was built up, indicated by a larger ratio between
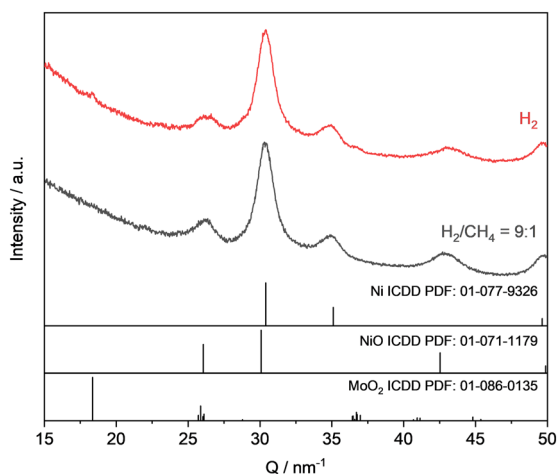
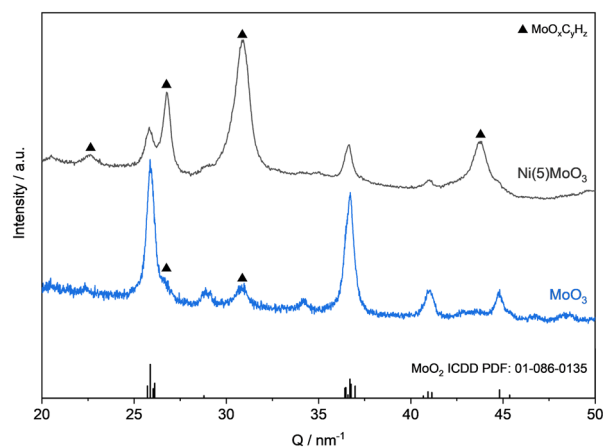**Fig. 10** Normalized long scan time *ex situ* XRD patterns for $NiMoO_4$ after *in situ* reduction in pure H_2 for 120 min and treatment in H_2/CH_4 (1:1) at 325 °C for 1200 min after no further changes in the diffractograms over time were observed.

Fig. 11 Normalized XRD results from the stepwise treatment of Ni(5)MoO_3 with H_2 and CH_4 at 325 °C compared with MoO_3.

2212 | *Catal. Sci. Technol.*, 2024, **14**, 2201–2217

This journal is © The Royal Society of Chemistry 2024

integral values for $MoO_xC_yH_z/MoO_2$. For comparison, Fig. 12 presents the *in situ* collected diffraction data of both experiments where MoO_3 is exposed to $H_2 : C_3H_6 = 9 : 1$ at 325 °C and $H_2 : CH_4 = 9 : 1$ at 350 °C. Note the unequal time scales, as the important changes occurred after different time intervals and previous diffractograms are not shown for better clarity.

During the *in situ* XRD experiment, in which C_3H_6 was used at 325 °C, after 120 min the reflections at $Q \approx 31$ nm^{-1} and $Q \approx 27$ nm^{-1} which belong to the oxycarbohydride phase can be identified (Fig. 12a). After 150 min a steady state seems to have been reached and comparatively strong intensity reflections of the $MoO_xC_yH_z$ phase, besides the reflections for MoO_2, were observable.

During the experiment with CH_4 at 350 °C (Fig. 12b) the formation began noticeably later after 190 min. Quasi-stationarity was reached after 230 min. Apparently, significantly more MoO_2 was formed compared to the experiment with propene.

For the interpretation of these results two aspects need to be considered. First, the slightly increased temperature during the experiment with methane could enhance the rate for the reduction of MoO_3 to MoO_2 to such an extent that the rate of carburisation is much lower in relation to this reduction step. Once the catalytically inactive MoO_2 is formed, it cannot be transferred into $MoO_xC_yH_z$.[24] This is because MoO_2 does not form molybdenum oxyhydride species (MoO_xH_y) which represents the precursor intermediate for the generation of $MoO_xC_yH_z$. Additionally, the lower reactivity of methane could be one reason for the significant over-reduction to MoO_2 because the carburisation of the partially reduced MoO_xH_y intermediate phase(s) might be slower with less reactive substrates. As already discussed for the nickel containing system Ni(5)MoO$_3$, improved reduction properties could be responsible for the enhanced formation of the $MoO_xC_yH_z$ phase, which is also feasible when using propene.[58] Thus, an activation treatment with a reactive hydrocarbon/hydrogen mixture could be promising to form significant amounts of

such an oxycarbohydride phase to generate a catalyst with enhanced activity and stability.

Catalyst regeneration by oxidative treatment

Another important aspect is catalyst regeneration by *in situ* oxidative treatment. It is known from the literature that the unpromoted MoO_3 catalyst possesses good regeneration properties when a calcination step is conducted.[14,46,48] Thus, we were interested to study the reoxidation behaviour of a nickel molybdate modified catalyst. During the reduction, the formation of a mixed-phase composition of the $NiMoO_4$ fraction occurs and the Ni^0 phase forms particles at the surface, a reformation of the nickel molybdate phase is possible in the course of oxidative treatment according to some reports.[39]

A sequential *in situ* XRD experiment was conducted with the Ni(1)MoO$_3$ catalyst material in which an intermittent reoxidation step was included. The sample was treated with a $H_2/C_3H_6 = 9 : 1$ mixture at 325 °C and after the formation of the $MoO_xC_yH_z$ phase, a gas mixture consisting of $O_2/He = 1 : 9$ was added for 4 h and then switched back to the initial hydrogen/propene mixture. The diffractogram of the starting material Ni(1)MoO$_3$ shows the reflections of MoO_3 and low intensity signals, related to the $NiMoO_4$ phase (Fig. 13). After the treatment with $H_2/C_3H_6 = 9 : 1$, pronounced broad reflections for the $MoO_xC_yH_z$ phase can be observed besides low intensity reflections for MoO_2. The reflection signals for $NiMoO_4$ and MoO_3 are not visible anymore.

After 4 h of oxidation, the reflections of MoO_3 and $NiMoO_4$ were detected again. However, tiny reflections of MoO_2 are still observable. Presumably, the temperature of
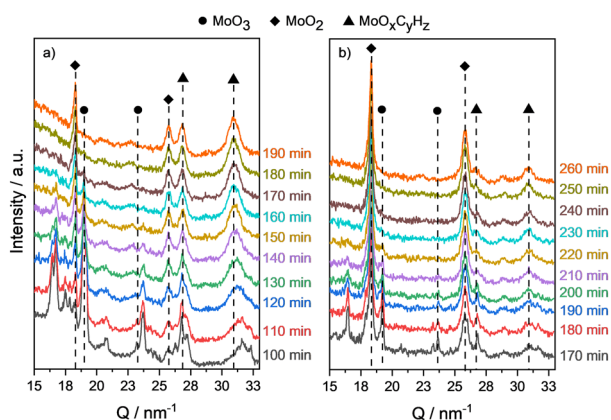

Fig. 12 Results from *in situ* XRD investigations on $MoO_xC_yH_z$ formation on MoO_3 with a) $H_2 : C_3H_6 = 9 : 1$ at 325 °C and b) $H_2 : CH_4 = 9 : 1$ at 350 °C.

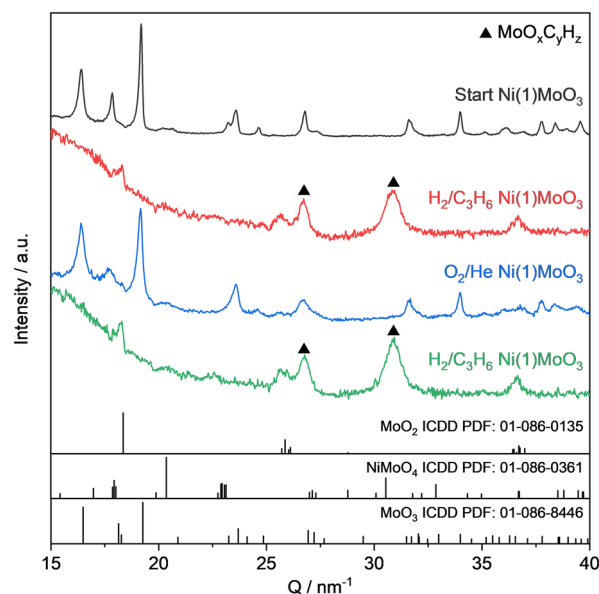**Fig. 13** Normalized *in situ* XRD-results from the monitoring of a stepwise active phase formation from Ni(1)MoO$_3$ with an intermittent reoxidation step at 325 °C for 4 h with O_2/He (1 : 9) and an H_2/C_3H_6 (9 : 1) mixture.

This journal is © The Royal Society of Chemistry 2024

Catal. Sci. Technol., 2024, **14**, 2201–2217 | **2213**

325 °C is not high enough for complete oxidation. Also, the reflections are less intense and sharp, which could be caused by an alteration in the microstructure during the reduction and oxidation, respectively. Nonetheless, by the second activation step the $MoO_xC_yH_z$ phase with similar large reflection intensities was formed. This is a good indication that regeneration of these catalysts is possible at least for a second cycle. Further experiments are required to study the impact of the temperature on the number of reoxidation cycles and the possible accumulation of inactive MoO_2. Also, the influence of the nickel content on catalyst recycling by reoxidation needs to be studied in more detail within the framework of succeeding research studies.[49,58]

Promotion of the $MoO_xC_yH_z$ phase formation by nickel

To acquire more insights about the beneficial role of lower nickel contents in the formation of the oxycarbohydride phase, a series of *in situ* XRD experiments were performed using $Ni(5)MoO_3$ and MoO_3 as reference materials in comparison to a physical mixture of NiO/MoO_3 and layers of NiO and MoO_3.

To carry out this experimental approach, we would like to discuss the following points. The obtained results with Ni(5)MoO_3, which showed the enhanced formation of the $MoO_xC_yH_z$ phase, could be related to the improved reducibility caused by nickel. It is important to mention that in the case of pure $NiMoO_4$ the population of the oxycarbohydride phase declined, presumably because of the significantly higher nickel content which could lead to the fast hydrogenolysis of the $MoO_xC_yH_z$ phase. Thus, moderately enhanced reduction properties caused by a lower nickel content seem to be beneficial, as this improves the formation of a molybdenum bronze (MoO_xH_y) in which the carbon is intercalated from the feed gas. For the potential case, activated hydrogen provided by a spillover effect would be responsible for the improved $MoO_xC_yH_z$ phase formation; also a local separation of MoO_3 from the H_2 activator (nickel) could result in a better formation of the oxycarbohydride phase.[24,52]

To address this hypothesis, the first *in situ* XRD experiment was conducted with the following procedure: a two-layer catalyst bed consisting of NiO (first layer) and MoO_3 (second layer) was prepared in the quartz capillary, in which the activated hydrogen created in the first layer could possibly lead to reduction and $MoO_xC_yH_z$ phase formation in the second layer by H_2-spillover. As a second control experiment, a physical mixture (MoO_3 + 5 wt% NiO) was also tested. Additionally, the reference catalysts Ni(5)MoO_3 and MoO_3 were investigated. The samples were treated for 5 h in a H_2/C_3H_6 mixture (9 : 1) at 325 °C.

For the sake of better comparison, the ratios of integral values for reflections of the target $MoO_xC_yH_z$ phase and the MoO_2 phase, which results from over-reduction, were calculated. In all samples, the formation of the oxycarbohydride phase began with the start of the reduction, resulting eventually in a mixture of $MoO_xC_yH_z$ with

reflections at $Q \approx 26.7$ nm^{-1} and 30.7 nm^{-1}, and for MoO_2 at $Q \approx 25.7$ nm^{-1} and 36.5 nm^{-1}, respectively (Fig. 14). As already discussed for the MoO_3 system, when C_3H_6 is used instead of CH_4, a significantly larger amount of the oxycarbohydride phase seems to be formed and the ratio of integral values for reflections at $Q \approx 26.7$ nm^{-1} denoted as $A(MoO_xC_yH_z)$ and at $Q \approx 25.7$ nm^{-1} denoted as $A(MoO_2)$, $R = A(MoO_xC_yH_z)/A(MoO_2)$ increases to $R = 1.5$ (for CH_4 this ratio was $R = 0.1$, see Table 3). When $Ni(5)MoO_3$ was used, considerably more $MoO_xC_yH_z$ phase is formed and a ratio of $R = 4.4$ was determined (Fig. 14a). Also, with methane the formation of $MoO_xC_yH_z$ with $Ni(5)MoO_3$ was promoted, resulting in a ratio of $R = 2.8$.

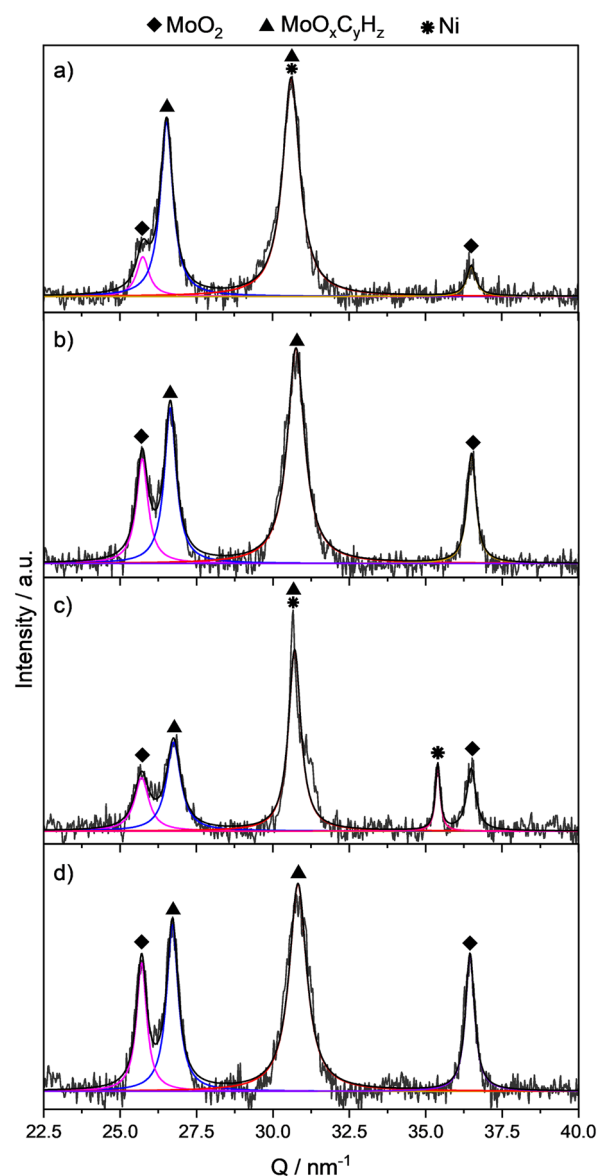Interestingly, when the nickel oxide was added as a layer above the MoO_3, the amount of the oxycarbohydride phase

Fig. 14 *In situ* XRD experiments of different samples at 325 °C in a gas mixture of H_2/C_3H_6 = 9 : 1 at TOS = 310 min. a) Ni(5)MoO_3; b) two layers of NiO/MoO_3; c) phys. mix of NiO/MoO_3; d) MoO_3.

Table 3 Ratio of integral values for reflections at Q = 26.7 nm^{-1} (MoO$_x$-C$_y$H$_z$) and Q = 25.7 nm^{-1} (MoO$_2$) of several *in situ* XRD experiments

Catalyst	Gas mixture	Ratio $A(\text{MoO}_x\text{C}_y\text{H}_z)/A(\text{MoO}_2)$
MoO$_3$	H$_2$/CH$_4$ (9:1)	0.1
MoO$_3$	H$_2$/C$_3$H$_6$ (9:1)	1.5
MoO$_3$ + NiO	H$_2$/C$_3$H$_6$ (9:1)	1.5
MoO$_3$ + NiO (phys. mix)	H$_2$/C$_3$H$_6$ (9:1)	1.7
Ni(5)MoO$_3$	H$_2$/C$_3$H$_6$ (9:1)	4.4
Ni(5)MoO$_3$	H$_2$/CH$_4$ (9:1)	2.8

remained constant (R = 1.5), compared to the pure MoO$_3$ in H$_2$/C$_3$H$_6$ (Fig. 14b *vs.* 14d). Because the H* migration could be hindered and not last until the end of the catalyst bed, the physical mixture of NiO and MoO$_3$ was tested. For this purpose, MoO$_3$ and 5 wt% of NiO have been mixed and pressed together to a particle size of 100–150 μm. From this experiment an integral ratio of R = 1.7 was obtained (Fig. 14c). In addition to the signals of MoO$_x$C$_y$H$_z$ and MoO$_2$, a reflection of metallic Ni was observed at Q = 35.4 nm^{-1}. It can be concluded that for both the layered system and the physical mixture, an improved oxycarbohydride phase formation could not be observed in these XRD experiments.

It is noteworthy that a reflection signal of metallic nickel was only observed for the physical mixture of NiO and MoO$_3$. Interestingly, such a nickel reflection was absent in the Ni(5)MoO$_3$ system, even though a reduction of the NiMoO$_4$ phase might lead to the formation of metallic nickel.[41] One reason for the absence of observable Ni reflections could be the formation of very small nickel particles which cannot be detected by XRD. A high dispersion of very small particles of Ni could be an explanation for the improved MoO$_x$C$_y$H$_z$ formation for nickel molybdate modified samples. One further effect could be the formation of an intermediate

mesoporous defective MoO$_{3-x}$ structure after the reduction, which could induce the formation of mixed-phases, increasing the tendency for an improved MoO$_x$C$_y$H$_z$ formation.[25,50]

These results reveal that improved H$_2$ activation by nickel is probably not the only reason for the enhancement of the oxycarbohydride phase formation. They rather indicate that the effects of different catalyst compositions (modification by NiO or NiMoO$_4$) and corresponding structural properties together with substrate properties, even though being different in nature, are most likely cumulative.

Conclusion

In molybdenum oxide based catalysts loaded with nickel or cobalt the transition metals are present as a binary structure of NiMoO$_4$ and CoMoO$_4$ combined with MoO$_3$, respectively. Catalysts with lower amounts of nickel up to a metal content of 5 wt% show higher activities towards the hydrodeoxygenation (HDO) of anisole with a slightly improved selectivity towards the aromatic products compared to pure phase MoO$_3$. The pronounced induction period observed for the unpromoted MoO$_3$ catalyst was increasingly shortened with increasing nickel content. Pure phase NiMoO$_4$ is the most active catalyst system and showed a further improvement of the selectivity for aromatic products. However, for NiMoO$_4$ a significantly high methane selectivity was also observed which indicates the decomposition of aromatic rings.

In situ XRD experiments showed that the formation of a molybdenum oxycarbohydride phase (MoO$_x$C$_y$H$_z$), which is found to stabilize the active Mo^{5+} sites preventing the over-reduction to inactive Mo^{4+}, is improved for the Ni modified catalysts with lower nickel contents (up to 5 wt%). For the pure nickel molybdate, the population of a MoO$_x$C$_y$H$_z$ phase
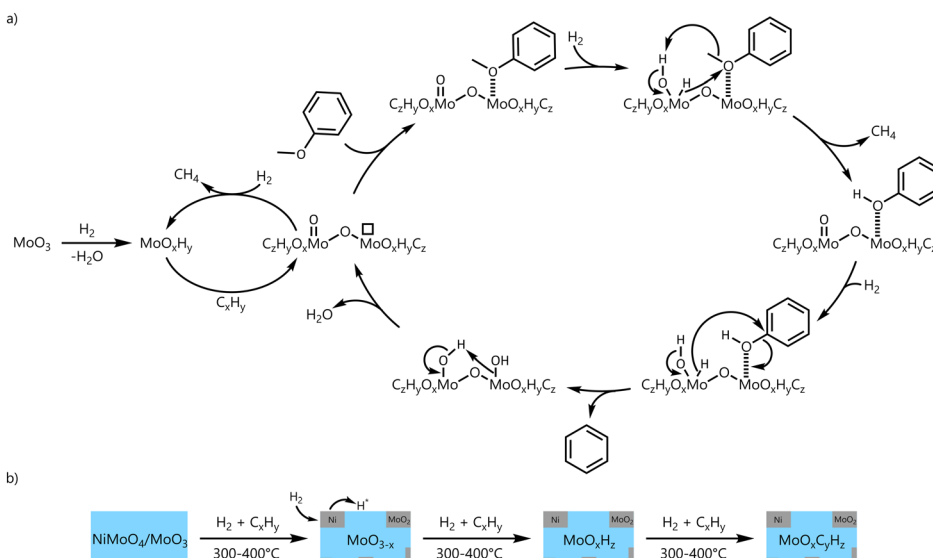
Scheme 4 Conclusive overall scheme for the HDO of anisole with MoO$_3$ (a) and a nickel molybdate modified catalyst (b).

This journal is © The Royal Society of Chemistry 2024

Catal. Sci. Technol., 2024, **14**, 2201–2217 | **2215**

could not be observed for samples treated in the presence of a hydrocarbon/oxygenate substrate and molecular hydrogen. Stepwise *in situ* DRIFTS-MS adsorption/hydrogenation experiments on $NiMoO_4$ indicated the decomposition of anisole and benzene over the pre-reduced nickel molybdate which could lead to a respective carbon containing phase such as $MoO_xC_yH_z$, which is hydrogenated to methane when exposed to pure hydrogen.

Catalytic control experiments in a fixed-bed reactor with $NiMoO_4$, $Ni(5)MoO_3$ and $Ni(3)/\alpha\text{-}Al_2O_3$ as catalysts and anisole and benzene as substrates revealed that the decomposition of arenes and the formation of methane could take place on a molybdenum and a nickel species simultaneously.

The formation of the molybdenum oxycarbohydride phase is effected by the substrate : hydrogen : molybdenum molar ratios as well as the reactivity of the substrate. The moderate reduction properties caused by a lower nickel content seem to balance the interplay between the enhanced reduction of molybdenum MoO_3 to MoO_xH_y phases – from which the $MoO_xC_yH_z$ phase is readily generated and stabilizes the active Mo^{5+} sites – and hydrogenolysis activity without leading to excessive over-reduction.

In Scheme 4, an extended catalytic cycle of the HDO of anisole with MoO_3 (a) and the formation steps of the oxycarbohydride phase $MoO_xC_yH_z$ starting from a nickel molybdate modified catalyst (b) are proposed. The established catalytic cycle can be complemented by the hydrogenation of incorporated carbon of $MoO_xC_yH_z$ in the formation of methane to MoO_xH_y which can be carburized again. In addition, the HDO *via* the reverse Mars–van Krevelen mechanism takes place at the Mo^{5+} sites which are distributed over $MoO_xH_y/MoO_xC_yH_z$ and are stabilized by the molybdenum oxycarbohydride phase.

Conflicts of interest

The authors declare no conflict of interest.

Acknowledgements

References

1 J. B. Zimmerman, P. T. Anastas, H. C. Erythropel and W. Leitner, *Science*, 2020, **367**, 397–400.
2 S. S. Wong, R. Shu, J. Zhang, H. Liu and N. Yan, *Chem. Soc. Rev.*, 2020, **49**, 5510–5560.
3 E. A. Agustiany, M. Rasyidur Ridho, M. Rahmi D. N., E. W. Madyaratri, F. Falah, M. A. R. Lubis, N. N. Solihat, F. A. Syamani, P. Karungamye, A. Sohail, D. S. Nawawi, A. H. Prianto, A. H. Iswanto, M. Ghozali, W. K. Restu, I. Juliana, P. Antov, L. Kristak, W. Fatriasari and A. Fudholi, *Polym. Compos.*, 2022, **43**, 4848–4865.
4 C. Liu, H. Wang, A. M. Karim, J. Sun and Y. Wang, *Chem. Soc. Rev.*, 2014, **43**, 7594–7623.
5 C. O. Tuck, E. Perez, I. T. Horvath, R. A. Sheldon and M. Poliakoff, *Science*, 2012, **337**, 695–699.
6 G. W. Huber, S. Iborra and A. Corma, *Chem. Rev.*, 2006, **106**, 4044–4098.
7 C. Li, X. Zhao, A. Wang, G. W. Huber and T. Zhang, *Chem. Rev.*, 2015, **115**, 11559–11624.
8 R. G. Ramirez Brenes, E. M. Alhadeff, N. Bojorge, L. E. M. Trales and G. A. D. Pazos, *Biofuels, Bioprod. Biorefin.*, 2023, **17**, 664–681.
9 J. L. Brito, A. L. Barbosa, A. Albornoz, F. Severino and J. Laine, *Catal. Lett.*, 1994, **26**, 329–337.
10 E. Furimsky, *Appl. Catal., A*, 2000, **199**, 147–190.
11 W. Jin, L. Pastor-Perez, D. K. Shen, A. Sepulveda-Escribano, S. Gu and T. R. Reina, *ChemCatChem*, 2019, **11**, 924–960.
12 J. H. Zhang, J. M. Sun and Y. Wang, *Green Chem.*, 2020, **22**, 1072–1098.
13 M. W. Nolte and B. H. Shanks, *Energy Technol.*, 2017, **5**, 7–18.
14 T. Prasomsri, M. Shetty, K. Murugappan and Y. Román-Leshkov, *Energy Environ. Sci.*, 2014, **7**, 2660–2669.
15 K. Murugappan, E. M. Anderson, D. Teschner, T. E. Jones, K. Skorupska and Y. Román-Leshkov, *Nat. Catal.*, 2018, **1**, 960–967.
16 V. O. O. Gonçalves, C. Ciotonea, S. Arrii-Clacens, N. Guignard, C. Roudaut, J. Rousseau, J.-M. Clacens, S. Royer and F. Richard, *Appl. Catal., B*, 2017, **214**, 57–66.
17 D. R. Moberg, T. J. Thibodeau, F. G. Amar and B. G. Frederick, *J. Phys. Chem. C*, 2010, **114**, 13782–13795.
18 M. Shetty, B. Buesser, Y. Román-Leshkov and W. H. Green, *J. Phys. Chem. C*, 2017, **121**, 17848–17855.
19 M. Rellán-Piñeiro and N. López, *ACS Sustainable Chem. Eng.*, 2018, **6**, 16169–16178.
20 D. Mei, A. M. Karim and Y. Wang, *J. Phys. Chem. C*, 2011, **115**, 8155–8164.
21 M. Shetty, E. M. Anderson, W. H. Green and Y. Román-Leshkov, *J. Catal.*, 2019, **376**, 248–257.
22 G. B. Báfero, G. B. Strapasson, D. S. Leite and D. Zanchet, *ChemCatChem*, 2023, **15**, e202300663.
23 A. J. Kohler, C. H. Walter and B. H. Shanks, *ACS Catal.*, 2023, **13**, 14813–14827.
24 C. Bouchy, C. Pham-huu and M. J. Ledoux, *J. Mol. Catal. A: Chem.*, 2000, **162**, 317–334.
25 P. Delporte, F. d. r. Meunier, C. Pham-Huu, P. Vennegues, M. J. Ledoux and J. Guille, *Catal. Today*, 1995, **23**, 251–267.
26 E. W. McFarland and H. Metiu, *Chem. Rev.*, 2013, **113**, 4391–4427.
27 H. Metiu, S. Chrétien, Z. Hu, B. Li and X. Sun, *J. Phys. Chem. C*, 2012, **116**, 10439–10450.
28 F. Yang, N. J. Libretto, M. R. Komarneni, W. Zhou, J. T. Miller, X. Zhu and D. E. Resasco, *ACS Catal.*, 2019, **9**, 7791–7800.

2216 | *Catal. Sci. Technol.*, 2024, **14**, 2201–2217

This journal is © The Royal Society of Chemistry 2024

29 J. Zhang, C. Li, W. Guan, X. Chen, X. Chen, C.-W. Tsang and C. Liang, *J. Catal.*, 2020, **383**, 311–321.

30 A. A. Smirnov, S. A. Khromova, D. Y. Ermakov, O. A. Bulavchenko, A. A. Saraev, P. V. Aleksandrov, V. V. Kaichev and V. A. Yakovlev, *Appl. Catal., A*, 2016, **514**, 224–234.

31 D. Raikwar, M. Munagala, S. Majumdar and D. Shee, *Catal. Today*, 2019, **325**, 117–130.

32 J. Zhang, C. Li, W. Guan, X. Chen, X. Chen, C.-W. Tsang and C. Liang, *Ind. Eng. Chem. Res.*, 2020, **59**, 4313–4321.

33 V. Itthibenchapong, P. Chakthranont, C. Sattayanon, T. Butburee, K. Faungnawakij and S. Namuangruk, *Appl. Surf. Sci.*, 2021, **547**, 149170.

34 C. Ranga, V. I. Alexiadis, J. Lauwaert, R. Lødeng and J. W. Thybaut, *Appl. Catal., A*, 2019, **571**, 61–70.

35 L. M. Madeira, M. F. Portela and C. Mazzocchia, *Catal. Rev.: Sci. Eng.*, 2004, **46**, 53–110.

36 O. Glemser and G. Lutz, *Z. Anorg. Allg. Chem.*, 1951, **253**, 17–33.

37 V. K. Pecharsky and P. Y. Zavalij, *Fundamentals of Powder Diffraction and Structural Characterization of Materials*, Springer Science & Business Media, New York, 2009.

38 J. T. Scanlon and D. E. Willis, *J. Chromatogr. Sci.*, 1985, **23**, 333–340.

39 H. M. Abdel-Dayem, *Ind. Eng. Chem. Res.*, 2007, **8**(46), 2466–2472.

40 J. E. Herrera and D. E. Resasco, *J. Phys. Chem. B*, 2003, **107**(16), 3738–3746.

41 J. A. Rodriguez, J. Y. Kim, J. C. Hanson and J. L. Brito, *Catal. Lett.*, 2002, **82**, 103–109.

42 Z. Song, T. Cai, Z. Chang, G. Liu, J. A. Rodriguez and J. Hrbek, *J. Am. Chem. Soc.*, 2003, **125**, 8059–8066.

43 J. L. Brito, J. Laine and K. C. Pratt, *J. Mater. Sci.*, 1989, **24**, 425–431.

44 W. J. Balfour, *Spectrochim. Acta, Part A*, 1983, **39**, 795–800.

45 H. Taghvaei, M. Kheirollahivash, M. Ghasemi, P. Rostami and M. R. Rahimpour, *Energy Fuels*, 2014, **28**, 2535–2543.

46 T. Prasomsri, T. Nimmanwudipong and Y. Román-Leshkov, *Energy Environ. Sci.*, 2013, **6**, 1732–1738.

47 P. Del Gallo, F. Meunier, C. Pham-Huu, C. Crouzet and M. J. Ledoux, *Ind. Eng. Chem. Res.*, 1997, **36**, 4166–4175.

48 C. Bouchy, C. Pham-Huu, B. Heinrich, C. Chaumont and M. J. Ledoux, *J. Catal.*, 2000, **190**, 92–103.

49 C. Bouchy, C. Pham-Huu, B. Heinrich, E. G. Derouane, S. B. Derouane-Abd Hamid and M. J. Ledoux, *Appl. Catal., A*, 2001, **215**, 175–184.

50 R. B. Patil, S. D. House, A. Mantri, J. C. Yang and J. R. McKone, *ACS Catal.*, 2020, **10**, 10390–10398.

51 C. Wang, L. Guo, K. Wu, X. Li, Y. Huang, Z. Shen, H. Yang, Y. Yang, W. Wang and C. Li, *J. Energy Chem.*, 2023, **84**, 122–130.

52 F. Roessner and U. Roland, *J. Mol. Catal. A: Chem.*, 1996, **112**, 401–412.

53 R. Prins, *Chem. Rev.*, 2012, **112**, 2714–2738.

54 R. Erre and J. J. Fripiat, in *Studies in Surface Science and Catalysis*, ed. G. M. Pajonk, S. J. Teichner and J. E. Germain, Elsevier, 1983, vol. 17, pp. 285–293.

55 G. Busca, *Phys. Chem. Chem. Phys.*, 1999, **1**, 723–736.

56 D. Nicosia, I. Czekaj and O. Kröcher, *Appl. Catal., B*, 2008, **77**, 228–236.

57 K. Cui, L. Yang, Z. Ma, F. Yan, K. Wu, Y. Sang, H. Chen and Y. Li, *Appl. Catal., B*, 2017, **219**, 592–602.

58 T. Ressler, J. Wienold, R. E. Jentoft and T. Neisius, *J. Catal.*, 2002, **210**, 67–83.

This journal is © The Royal Society of Chemistry 2024

Catal. Sci. Technol., 2024, **14**, 2201–2217 | **2217**